Structural Anisotropy Governs the Kink Formation in Cellulose Nanocrystals

Jia Hui Lim, Yun Jing, Sung Park, Yoshiharu Nishiyama, Muriel Veron, Edgar Rauch, Yu Ogawa

Structural Anisotropy Governs the Kink Formation in Cellulose Nanocrystals

*Jia Hui Lim,[1] Yun Jing,[2] Sung Park,[2] Yoshiharu Nishiyama,[1] Muriel Veron,[3] Edgar Rauch,[3] and Yu Ogawa [1]**

[1] Univ. Grenoble Alpes, CNRS, CERMAV, 38000 Grenoble, France

[2] Molecular Vista Inc., 6840 Via Del Oro, Suite 110, San Jose, CA 95119, USA.

[3] Univ. Grenoble Alpes, CNRS, Grenoble INP, SIMaP, F-38000 Grenoble, France

*Email: yu.ogawa@cermav.cnrs.fr

ABSTRACT

Understanding the defect structure is fundamental to correlating the structure and properties of materials. However, little is known about the defects of soft matter at the nanoscale beyond their external morphology. We report here on the molecular-level structural details of kink defects of cellulose nanocrystals (CNCs) based on a combination of experimental and theoretical methods. Low-dose scanning nanobeam electron diffraction analysis allowed correlating the local crystallographic information and nanoscale morphology and revealed that the structural anisotropy governed the kink formation of CNCs. We identified two bending modes along different crystallographic directions with distinct disordered structures at kink points. The drying

strongly affected the external morphology of the kinks, resulting in underestimating the kink population in the standard dry observation conditions. These detailed defect analyses improve our understanding of the structural heterogeneity of nanocelluloses and contribute to the future exploitation of soft matter defects.

TOC GRAPHICS

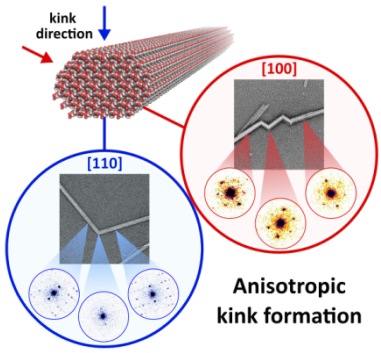

KEYWORDS

Cellulose; Defect; Kink; Electron diffraction; Scanning transmission electron microscopy.

Cellulose nanoparticles, including cellulose nanocrystals (CNCs) and nanofibers (CNFs), are a class of fibrous crystalline nanomaterials extracted from cellulosic biomass (e.g., land plants). These so-called nanocelluloses have attracted significant attention as a bio-sourced alternative to synthetic materials for their abundance, renewability, low toxicity, and excellent material properties.[1] Extensive research efforts have been made in the structural and morphological characterization of these nanoparticles to understand their structure-properties relationships. Such characterization focused chiefly on the size estimation of the nanoparticles.[2–4] While the

other finer morphological details, including various defects, have long been observed in the literature,[5–7] they have only recently received closer scrutiny on their structural aspects.[8–11]

One of such underexplored features of nanocelluloses is kink defects, i.e., sharp bends along the fiber axis of the nanoparticles. Kinks are common defects in fibrous materials, from carbon nanotubes and amyloid fibrils to macroscopic cellulose fibers.[12–14] TEM and atomic force microscopy (AFM) observations have revealed that the kink is a widespread morphological feature of nanocelluloses regardless of the type of nanoparticles, processing conditions, or the source of cellulose.[10,15–19] Various possible functions have been proposed for the kinks, from a mechanical weak point to an active site for chemical and enzymatic modification of nanocelluloses.[17,18,20–22] While they undoubtedly have consequences on the material properties of nanocelluloses, their actual functionalities remain largely hypothetical due to the lack of understanding of their ultrastructure. The current knowledge is based solely on morphological observations. For instance, the previous studies proposed extensive chain breakages at the kink points,[21,22] but such molecular-level structural changes are not detectable by morphological characterization. On the other hand, molecular modeling provided insights into molecular details of the kinks. Molecular dynamics (MD) simulations suggest that the bending of cellulose crystals is highly anisotropic due to the molecular packing of the cellulose crystal.[23] The mechanical anisotropy of cellulose presumably affects the kink formation of nanocelluloses. However, its implication has been overlooked due to the lack of a suitable characterization technique that can connect the internal crystal structure to the external kink morphology of cellulose.

Here, to better understand the structure-properties relationship of the kink defects of nanocelluloses, we investigated the structure of the kinked CNCs using scanning nanobeam electron diffraction analysis (SNBED). The technique derived from the Automated Crystal

Orientation Mapping (ACOM) approach pioneered in the 1990s[24] and further developed as ASTAR® tool.[25] The method recently extended to a broader range of four-dimensional scanning TEM (4D STEM) techniques.[26] The SNBED analysis allows us to obtain spatially resolved crystallographic information by scanning over the sample with a focused electron beam.[27–29] Based on the local structural information from the SNBED data, we reveal the molecular-level details of the kink structure of CNCs. We demonstrated that the observed kink morphology of CNCs results from the interplay between the structural anisotropy of CNCs and the drying step during the sample preparation. The SNBED results combined with a nanoscale chemical mapping based on AFM-infrared (AFM-IR) spectroscopy and molecular modeling also allowed us to shed light on the structural disorganization at the kink points and the origin of the kink defect formation.

This study used tCNCs obtained via sulfuric acid hydrolysis of purified tunicate cellulose. Tunicate cellulose is a model cellulose specimen consisting of large crystallites, the crystal structure of which is composed of the monoclinic Iβ allomorph exclusively (Fig. S1A-C).[30] Figure 1A illustrates the straight fibrillar morphology of tCNCs with only occasional kinks (arrowhead in Fig. 1A). tCNCs have a fibril width of typically around 12-15 nm and a length of about one micron (Fig. S2). The cross-section of tCNCs is an elongated octagon (Fig. 1E) with the (1 -1 0) surface as a major facet and the (1 1 0), (1 0 0), and (0 1 0) surfaces as minor ones (Fig. S1D).[31] As described by Helbert and co-workers,[31] this cross-sectional shape results from acid hydrolysis that preferentially peeled off the chains at the acute corners of the original parallelogram cross sections. While tCNCs regularly twist in the aqueous suspension, they alter their morphology to a flat ribbon shape when dried on a flat hydrophilic surface due to the surface tension of water and the surface interactions between tCNCs and the substrate.[8] This

drying effect resulted in only a few possible orientations of tCNCs on the substrate, as shown in the SNBED orientation map (Fig. 1B). The majority of tCNCs (75%) lie flat on the wider surface (Fig. 1E). This orientation corresponds to the [1 -1 0] zone-axis diffraction pattern (Figs. 1C and 1D, red signals in Fig. 1B). The minority (25%) lies on the narrower (0 1 0) face (Figure 1H), corresponding to the [0 1 0] zone-axis ED pattern (Figs. 1F and 1G, green signals in Fig. 1B).

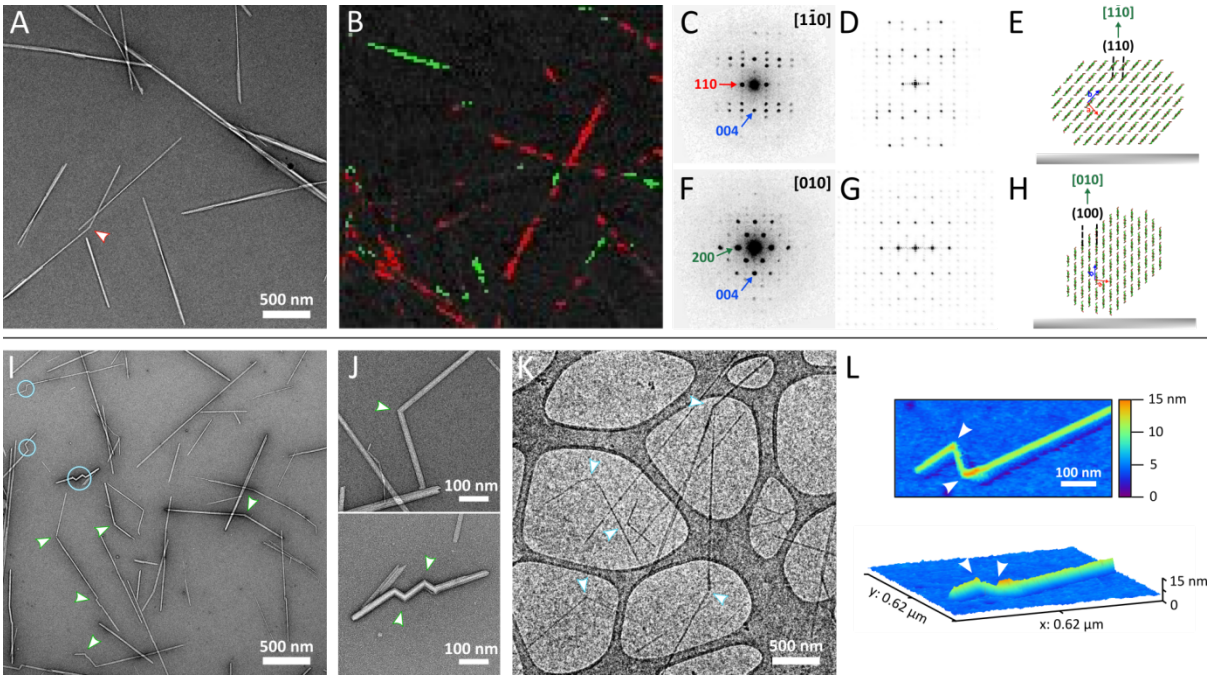

Figure 1. Overview of untreated and kinked tunicate cellulose nanocrystals (tCNCs). (A) TEM image of negatively stained tCNCs. (B) VDF image of straight tCNCs. The two crystallographic orientations, [1 -1 0] and [0 1 0], correspond to red and green pixels, respectively. (C) ED pattern of a straight fibril along [1 -1 0] zone axis and (D) its corresponding simulated diffraction pattern. (E) Molecular model of a cross-section of tCNC with [1 -1 0] zone axis perpendicular to the carbon support film and parallel to the electron beam. (F) ED pattern of a straight fibril along the [0 1 0] zone axis and (G) its corresponding simulated diffraction pattern. (H) Molecular model of a cross-section of tCNC with [0 1 0] zone axis perpendicular to the carbon support film and parallel to the electron beam. (I) TEM image of negatively stained tCNCs after

ultrasonication treatment. Arrowheads point to single kinks, and circles indicate zigzag kinks. (J) Zoomed-in images of single (top) and zigzag kinks (bottom). (K) cryo-TEM image of tCNCs after ultrasonication treatment. Arrowheads indicate kink points. (L) AFM topography image of zigzag kinks (top) and a 3D image (bottom) showing the thickening of fibril at the kink.

We then applied ultrasonic radiation to induce kink defects in tCNCs. After the ultrasonication, more kinks were present in tCNCs under the standard dry (Fig. 1I) and the cryogenic conditions (Fig. 1K) that preserved the native aqueous suspension state. The kink occurred due to the bending forces generated by the ultrasonication-induced cavitation jet.[32] The morphological observations showed two distinct modes of kinks, single and zigzag kinks. The former represents an individual and isolated kink (Fig 1J top). The latter corresponds to successive bends separated with straight segments typically less than 100 nm long (Fig. 1J bottom). The distributions of the kink angle (as defined in Fig. S3) differed depending on the kink modes as described below. The AFM images show altered 3D morphology of tCNCs around the kinks (Figs. 1L and S4). The nanocrystals laterally expanded around the kinks, as seen in the increase in the fibril height. This lateral deformation indicates that the kinks of tCNCs are three-dimensional defects in contrast to other simpler nanoscale kink defects, e.g., those of carbon nanotubes often considered as 2D defects.[14,33]

These observations revealed the fine details of the kink defects of tCNCs. However, it is impossible to correlate these morphological features with the local molecular organization based solely on the morphological analyses. It is unclear whether and how the two kink modes relate to the crystal structure of cellulose and if the morphological change of the crystal is indicative of internal molecular disorganization.

We performed the SNBED analysis on the kinked tCNCs to obtain local crystallographic information around the kinks. We reduced the radiation dose per scan position to the critical dose for cellulose crystal, ca. 4 e^-/A^2,[34] to obtain high-resolution ED patterns. Figure 2 shows SNBED datasets where 2D ED patterns were recorded at each pixel position of 2D scan maps (Fig. 2B and 2E). The ED patterns of the straight segments are generally of high resolution, often beyond 2 Å (Fig. 2). Thanks to the low dose acquisition and highly sensitive direct electron detector, weak diffraction intensities were detectable in the disorganized areas. Based on these SNBED datasets, we could unambiguously determine the crystallographic bending direction and the structural disorganization of the kinks. Such information allowed us to correlate the internal molecular organization to the external morphology.

Figures 2A (Virtual bright field, VBF and virtual dark field, VDF images - defined in the supporting information) and 2B (ED patterns) show a dataset obtained from a tCNC with a single kink, while Figures 2D and 2E are that of zigzag kinks. The ED patterns of the former are all [1 -1 0] zone-axis patterns, indicating the bending direction of the kink is along [1 1 0] zone axis (Fig. 2C). The straight segments of the zigzag kinks have identical crystallographic orientation, yielding the [0 1 0] zone-axis pattern (Fig. 2E). The bending of the zigzag kinks is thus along the [1 0 0] zone axis (Fig. 2F). Other examples of SNBED data of kinked tCNCs are available in the supporting information (Fig. S5-S7). Among 59 kinks analyzed by the SNBED method, 55 kinks had the same crystallographic orientations on both sides of the kinks. Most kinked nanocrystals thus lay flat on the carbon surface without rotation at the kinks. The other minor kinks showed different ED patterns on neighboring straight segments, indicating the twist of the crystals at the kinks (Fig. S8).

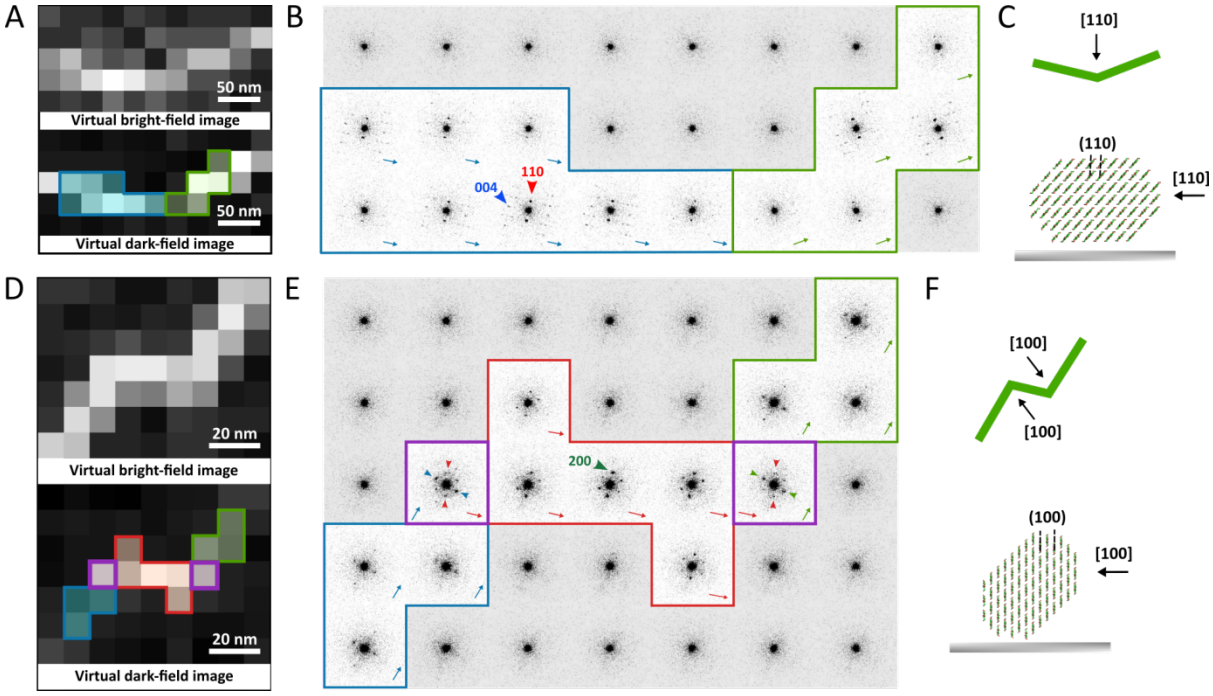

Figure 2. Scanning nanobeam electron diffraction (SNBED) analysis of kinked tCNCs. (A) Virtual bright field (VBF) (top) and virtual dark field (VDF) (bottom) images of a single kink with an angle of 33°. (B) ED patterns along the kinked tCNC in (A). Arrows on the bottom right of each ED pattern indicate the fiber axis. (C) Schematic illustration of single kink mode bent along [1 1 0] zone axis. (D) VBF (top) and VDF (bottom) images of zigzag kinks with angles of 72°(left) and 73° (right). (E) ED patterns along the kinked tCNC in (D). ED patterns in purple boxes show superimpositions of two ED patterns with different fiber orientations. (F) Schematic illustration of zigzag kink mode bent along [1 0 0] zone axis.

We could correlate the crystallographic bending directions with the kink angle distribution. The morphology-based kink angle distribution in the dry condition is asymmetric and bimodal with peaks at 20° and 60° (Fig. 3A). The two kink modes, single and zigzag, have different distributions: the former has a broad asymmetric distribution with primary and secondary peaks

at 20° and 60°, respectively, while the latter has a narrower distribution centered at 70° (Fig. 3B). The overall kink angle distribution (Fig. 3A) is similar to the one based on the AFM of dry wood cellulose nanofibrils, having a peak at 60°.[10] Molecular modeling studies predicted the plastic deformation limit of bending of cellulose at around 60°.[23,35] The presence of the plastic limit may partially explain the peak position at 60° since the kink of tCNCs may be stabilized at the plastic limit angle. The distinct distributions of the two kink modes imply structural differences between the two kink modes.

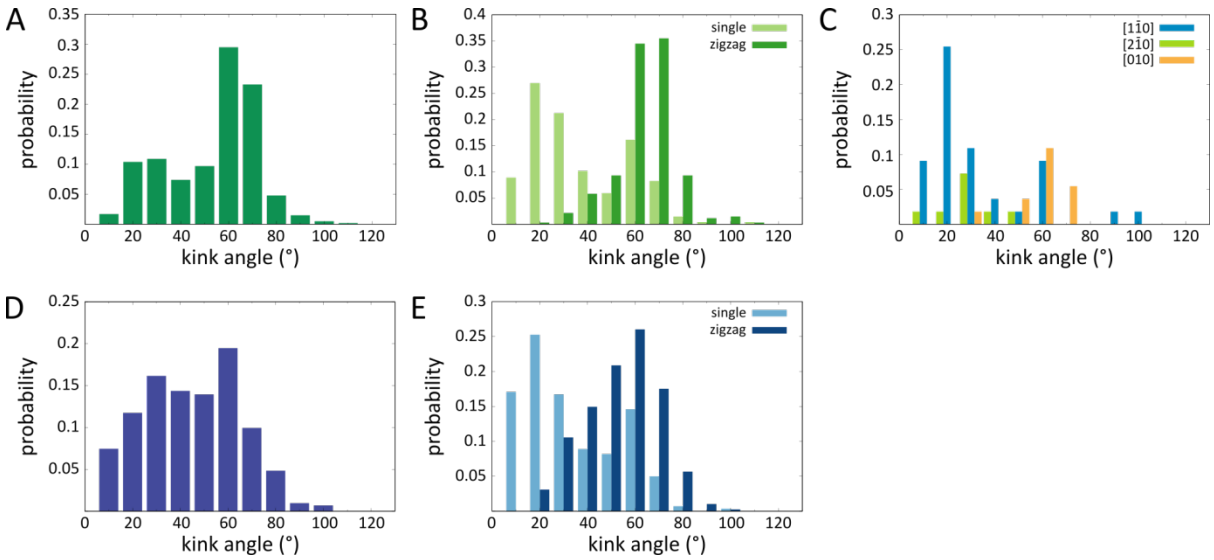

Figure 3. Kink angle distributions based on morphological and SNBED analyses in dry and cryo conditions. (A) Kink angle distribution based on the morphology of kinked tCNCs dried on carbon supporting film. (B) same as (A), but single and zigzag kinks are plotted as separate datasets. (C) Kink angle distribution derived from SNBED analysis of tCNCs dried on carbon supporting film. (D) Kink angle distributions based on the morphology of kinked tCNCs embedded in vitreous ice layer (cryo-TEM). (E) same as (D) but single and zigzag kinks plotted as separate datasets.

The SNBED patterns recorded around the kinks showed only a limited number of crystallographic orientations yielding the [1 -1 0] and [0 1 0] zone-axis patterns with a minor [2 -1 0] pattern (Fig. 3C, S9). They correspond to the two kink morphologies. The kinks of the [1 -1 0] and [2 -1 0] patterns are single kinks, while those of the [0 1 0] pattern are zigzag kinks. The kink angle distributions are consistent between the morphological and SNBED analyses. The single kinks with [1 -1 0] and [2 -1 0] have broad distributions with peaks at around 20°, and the zigzag kinks with [0 1 0] pattern have a narrow distribution centered at 60° (Fig. 3C). Considering the rare occurrence and the similar morphology, we speculate that the crystals yielding [2 -1 0] pattern shared the same kink geometry with those of [1 1 0] but with a slight tilt around the fiber axis. The angle between [1 1 0] and [2 -1 0] zone axes is 14° (Fig. S9). Such a slight rotation may arise from the local distortion of the carbon supporting film.

Based on the above consideration, we identified the two kink modes for tCNCs, when in the dry condition: the single kinks bent along the [1 1 0] zone axis (Fig. 2C) and the zigzag ones bent along [1 0 0] zone axis (Fig. 2F). The [1 1 0] mode is predominant (80%) in the diffraction analysis. These discrete kink modes indicate that the anisotropic structure of cellulose crystal governs the kink formation of tCNCs. On the other hand, considering the process used in this study, it is counterintuitive to find only two kink modes. Most kinks were generated by ultrasonication of the suspension where tCNCs could freely rotate. This situation should result in a larger number of kink modes along different crystallographic directions.

Furthermore, the predominance of the [1 1 0] mode is apparently inconsistent with the mechanics of the cellulose crystal. The kink formation is a complex deformation process as the material goes through elastic and plastic deformations and eventual failure. The failure process of cellulose is underexplored to date at the molecular level. Thus, here we discuss the kink

formation mechanism based on the elastic and plastic deformation corresponding to the initial stage of the kink formation. The MD simulations estimated the flexural moduli of the crystal parallel to four major zone axes in the following order: [0 1 0] > [1 1 0] ≃ [1 -1 0] > [1 0 0].[23] The cross-sectional shape of the nanocrystals also affects the bending behavior. As shown in Fig. 1E, the ratio of the long to short axes of the cross-section is about 1.6:1.[36] The second moment of inertia is thus about 2.5 times larger in the bending along [1 1 0] compared to that along [1 -1 0], as described in the supporting information file (Fig. S10). The bending along [1 -1 0] is thus mechanically more favorable to the [1 1 0] mode, despite the former's absence and the latter's predominance in our experiments.

This apparent discrepancy between the experimental observations and the mechanics-based prediction likely arises from the drying of tCNCs on the flat substrate (Fig. 4). As aforementioned, the non-kinked tCNCs tend to lie flat on the long (1 -1 0) side when dried on a flat surface. This tendency should persist with the presence of the kinks as the local interactions remain the same among the tCNC surfaces, water, and carbon substrate. Here, we consider two possible cases (Fig. 4). When the kink is parallel to the longer side of the cross-section, along [1 1 0] (Figs. 2C, 4A), the crystal lies in the preferred orientation without geometric conflict since both straight segments of the kink remain in-plane of the flat surface and the (1 -1 0) facet. The kinks maintain their morphology in the suspension upon drying (Fig. 4B). When the kink is in other directions (Fig. 4C), there is a geometric conflict since either straight segment has to be out-of-plane with the (1 -1 0) facet. If the kink angle is below the plastic limit, the drying force, mainly the surface tension pulling the crystal to the substrate, straightens the kinked crystal (blue arrowhead in Fig. 4D). It allows the straightened crystal to lie in the preferred orientation. Conversely, when the kink angle exceeds the plastic limit, the crystal remains bent even when

the drying force is applied. The crystal rotates and settles in a different orientation, so both straight segments are in-plane with the substrate plane. This proposed mechanism is presumably why the non-[1 1 0] mode is mainly populated with a bending angle above 60° (Fig. 3C). The fact that the [1 0 0] mode is the only observed non-[1 1 0] mode is likely because it is the bending direction with the lowest flexural modulus.[23] The probability is the highest for the crystals to bend beyond the plastic limit along the [1 0 0] direction.

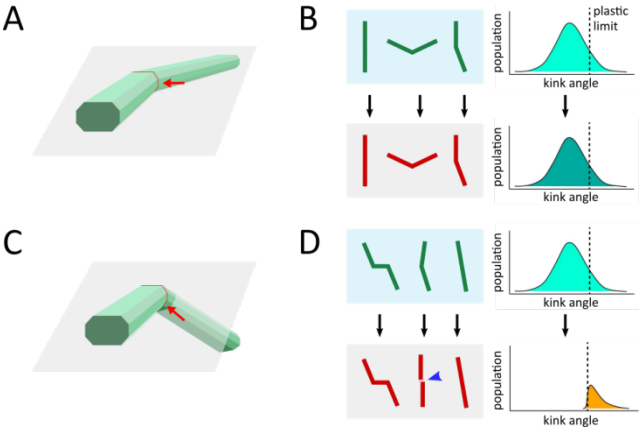

Figure 4. Effect of drying on the kink morphology of tCNCs. (A) Schematic illustration of tCNC bent along [1 1 0]. The bending direction is in-plane with the long (1 -1 0) surface. (B) Morphology (left) and kink angle distribution (right) of tCNCs bent along [1 1 0] in the suspension (top) and dry conditions (bottom). Both morphology and distribution are unaffected by the drying. (C) Schematic illustration of tCNC bent along non-[1 0 0] direction. The bending direction is out-of-plane with the long (1 -1 0) surface. (D) Morphology (left) and kink angle distribution (right) of tCNCs bent along non-[1 1 0] in the suspension (top) and dry conditions (bottom). The low-angle kinks are straightened upon drying (indicated by the blue arrowhead). The kinks above the plastic limit remain kinked, resulting in a biased kink angle distribution.

In summary, drying is one of the principal factors in determining the kink morphology of tCNCs, together with the structural and mechanical anisotropy of cellulose crystals. The drying force likely suppresses non-[1 1 0] kinks with a kink angle below the plastic limit, which reduces the number of kinks and alters the kink angle distribution compared to those in the original suspension state. To examine this hypothesis, we determined the kink angle distribution of tCNCs in the cryo condition (Fig. 3D). We found a broader kink angle distribution in the cryo condition with a larger kink population at the lower kink angle. In particular, the distribution of the zigzag kinks was strongly affected by drying, as the one in the cryo condition had more kinks below 50° (Fig. 3E).

The local structural information obtained from the SNBED analysis allowed us to determine the structural disorganization features of the two kink modes. The diffraction intensities significantly weakened around the single kinks (Fig. 2A, 5B, and S6), indicating the partial loss of crystallinity around the kink. The disorganized area typically extended 20-50 nm along the fiber axis on both sides of the kinks (Fig. 2A, S6). The intensity loss of the 1 1 0 reflection was often more significant than the meridional 0 0 4 reflection (Fig. 2B, S5, S6). The molecular packing was thus more disorganized in the lateral plane of the crystal than along the fiber axis. While the MD model showed similar lateral disorganization around the kink point,[23] the effect was more significant in the experiment as the simulated pattern showed relatively strong diffraction intensities at the kink (Figure 5B, bottom).

In the straight segments next to the single kinks (Fig. 2A, 5A, and S6), ED patterns were often asymmetric with strong diffraction intensities only in two diagonal quadrants (Fig. 2A and 5B position 1), contrary to the symmetric ones of the straight tCNCs (Fig. 1C). To understand this asymmetry, we simulated diffraction patterns of the MD-simulated crystal bent along the same [1

1 0] direction (Fig. 5A, right). The pattern of the straight segment (position 1) next to the bending point shows a similar asymmetry (Fig. 5B, bottom). At this bending angle of 20°, the deformation of the simulated crystal is above the linear elastic limit, where the shear strains become more significant compared to the axial strains.[23] The shear strain is likely the cause of asymmetry in the diffraction pattern, as the crystal below the linear elastic limit did not show an asymmetric pattern (Fig. S11). The crystal was thus largely shear-deformed at 100 nm away from the kink. This observation indicates that the kinks affect the internal structure of the straight segments without altering the external morphology. Such large shear deformation often occurs only on one side of the kink. The diffraction pattern on the other side of the same kink was more symmetric (Figure 5A, position 3), consistent with the MD-simulated diffraction pattern. The asymmetry of shear deformation was also observed in our previous report on the MD simulations of bending of cellulose, which induced a local allomorph conversion.[37]

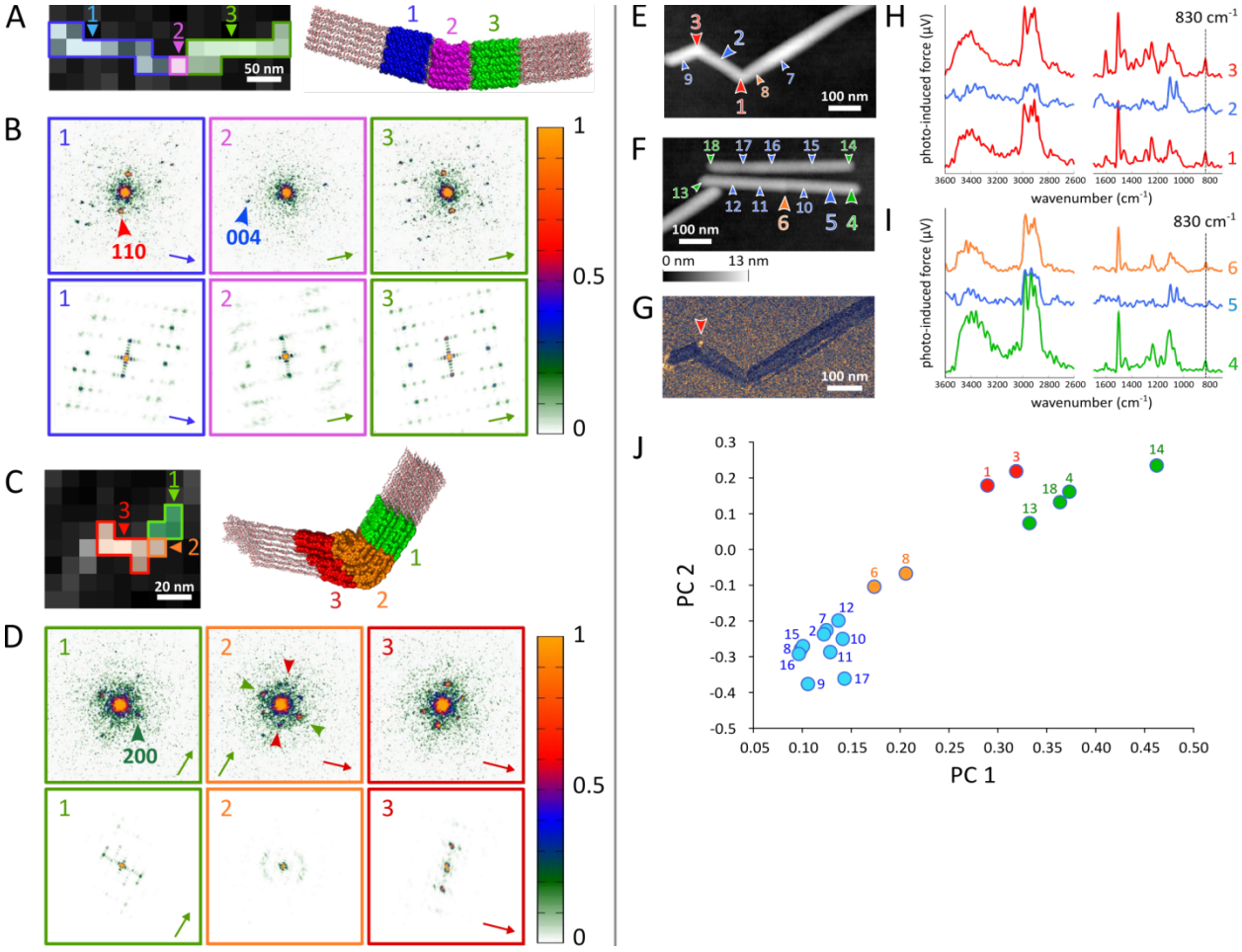

Figure 5. Local molecular organization at the kink points analyzed by SNBED, MD simulations and PiFM. (A) VDF image (left) of tCNC with a [1 1 0] kink of an angle of 20° and a molecular model based on force field molecular dynamics (MD) simulation (right) of cellulose crystal bent along [1 1 0]. (B) Experimental (top) and simulated (bottom) diffraction patterns at different locations indicated by boxes with corresponding colors in (A). (C) Virtual dark-field (VDF) image (left) of tCNC with [1 0 0] kink of an angle of 72° and a MD-simulated molecular model (right) of cellulose crystal bent along [1 0 0]. (D) Experimental (top) and simulated (bottom) diffraction patterns (bottom) at different locations indicated by boxes with corresponding colors in (C). The color gradient in (B) and (D) corresponds to the relative intensities of ED spots. (E, F) AFM topography image of kinked and straight tCNCs. (G) Spectral map at 830 cm^{-1}, a

characteristic band of the sulfate half-ester group. (H, I) Local PiF-IR spectra obtained from (H) kinked and (I) straight tCNCs indicated by arrowheads in (E) and (F). (J) PCA score plot of the two first principal components (PC1 & PC2) based on 18 PiF-IR spectra obtained from positions indicated in A and B.

The deformation manner of the zigzag kinks along [1 0 0] significantly differs from the single one, where two straight crystalline segments are connected at the kink point without an extensive disorganized area (Figure 2B, 5C, S7). At the kink point (Figure 5D, position 2), the ED pattern contained two sets of ED patterns of different orientations (indicated by red and green arrowheads). This superimposed ED pattern suggests that the crystalline order of tCNC was well preserved even within the area with a diameter of 10 nm (i.e., the spot size) around the kink point. On the other hand, in the kink position of the MD model (Fig. 5C - right), the simulated pattern shows more smeared diffraction spots compared to the experimental ones (Fig. 5D, bottom), indicating an overestimation of the disorganization effect in the MD model.

The apparent lack of the disordered region in the [1 0 0] mode might be due to the limited spatial resolution of our SNBED experiments, ca. 10 nm. To overcome this lack of resolution, we thus used an AFM-IR chemical mapping method known as Photo-induced Force Microscopy (PiFM).[38] We acquired a 2D IR spectral map with a spatial resolution of sub 5 nm (Fig. 5E-5J). The topography image of tCNCs with zigzag kinks and those without apparent kinks are shown in Figures 5E and 5F with associated IR spectra in Figures 5H and 5I. The width of tCNCs appeared to be about 40 nm, more than twice as wide as the average value, 13 nm. This overestimation was due to the tip-broadening effect in the AFM measurement and was consistent with the typical radius of curvature of ~ 25 nm for the metal-coated AFM tip.

We then performed principal component analysis (PCA) of the PiF-IR spectra to compare the local molecular environments of straight and kinked areas of tCNCs. Figure 5J shows a PCA score plot of the two first principal components (PC1 and PC2) of 18 PiF-IR spectra of the positions indicated in the topography images (Fig. 5E, 5F, S12). Sub-spectra of PC1 and PC2 are available in Figure S13. There are three clusters. The left cluster contains only the straight segments (blue plots), while the small middle one is composed of straight segments with structural disorganization, as further discussed below. The right cluster consists of the crystal extremities (green) and kinks (red). The cluster pattern indicates that the kinks share spectral features with the extremities that are significantly different from those of the straight segments. The local molecular environment of the kinks is thus similar to that of the extremities, implying the higher exposure of molecular chains and possible chain breakage localized at the kinks.

The increase of band intensity at 830 cm^{-1} was the prominent feature of the kinks and the extremities (Fig. 5H and 5I). The band corresponds to the sulfate half-ester groups induced by sulfuric acid hydrolysis. There was an accumulation of sulfate half-ester groups at one of two kinks similar to the extremities (red arrowhead in Fig. 5G). As the esterification occurred only during the hydrolysis,[39] this kink most likely formed before or during the hydrolysis. The other kink showed no evident accumulation of sulfate half-ester groups and thus formed after hydrolysis, likely during ultrasonication. The area of this accumulation corresponds to the molecular disorganization in the zigzag kinks. It extended less than a quarter of the width of the tCNCs, implying the disorganization of zigzag kinks localized in an area with a diameter smaller than 4 nm.

The combination of SNBED and PiFM revealed the distinct structural disorganization manners of the single and zigzag kinks. PiF-IR mapping enabled us to locate the disordered region with a

sub-5 nm resolution, previously unattainable based on other AFM- or EM-based methods.[40,41] Our analyses demonstrated the disorganization of lateral molecular packing in the [1 1 0] mode, consistent with the bulk solid-state NMR observations of sonicated cellulose nanoparticles.[22,32] On the other hand, no extensive breakage of the crystals was observed even at the high kink angle, unlike the previous assumption based on the morphological analyses.[21] This observation, however, does not exclude the possibility that the kinks behave as active sites of chemical and enzymatic reactions on cellulose crystals. A PiF-IR image showed water accumulation at the kink positions (Fig. S15E), indicating the altered surface property and potentially higher chemical reactivity.

The drying-induced preferential orientation of tCNCs strongly affected the observed kink morphology. This drying artifact likely resulted in underestimating the number of kinks, which can lead to inaccurate statistical analysis of other morphological parameters, e.g., contour length. Considering that the dry condition is a standard observation condition of TEM and AFM, the drying artifact significantly degrades the representativeness of the defect analyses of nanocelluloses. It is thus necessary to perform the structural investigation under non-dry conditions (cryo and liquid state conditions) for a better understanding of the structure-properties relationships of the defects of nanocelluloses.

Our observation also indicates the kinked cellulose crystals have structural flexibility to recover the straight morphology upon drying. There were apparent traces of the straightened kinks as slight displacements of two straight segments (Fig. S14). These displacement defects were present only in the kinked tCNCs observed in the dry condition. A similar kink trace appeared in the topology image of the PiFM analysis (position 6, Fig. 5F). The spectrum shows similarity to those of kinks (Fig. 5I). The PCA analysis locates it between the straight and

extremity clusters (Fig. 5J) and thus indicates straightened kink trace likely has local molecular disorganization. This observation suggests that once the kink forms in the cellulose crystal, the local molecular disorganization remains even when the external morphology is straight. The drying artifact would thus also result in underestimating the disorganized areas in nanocelluloses.

Shear deformation caused by the bending of cellulose has been associated with the occurrence of two allomorphs of native cellulose, i.e., Iα and Iβ. Previous studies suggested that the shear stress during cellulose biosynthesis may give rise to the energetically less stable Iα allomorph.[42,43] In this study, however, we did not observe any diffraction pattern of the Iα allomorph in the vicinity of the kinks where the crystal was under substantial shear stress. Our previous MD study showed that the shear-induced conversion from Iβ to Iα is only transitory, while that from Iα to Iβ is progressive and cumulative.[37] The lack of the Iα phase in our study is consistent with the MD results and may imply the presence of another mechanism for the biogenesis of the Iα allomorph.

In conclusion, our study sheds light on the molecular-level structural details of the kink defects of cellulose nanocrystals and their formation mechanisms. The structural anisotropy of cellulose is the principal factor to govern the kink formation of tCNCs, resulting in the two discrete kink modes along the [1 1 0] and [1 0 0] directions. The observed morphology of kinks was strongly affected by the drying-induced preferential orientation of tCNCs. This observation revealed the critical consequence of drying, a standard sample preparation process, in the observed external morphology of soft nanomaterials.

The nanoscale defects of soft materials are largely underexplored compared to those in hard solids, partially due to the lack of suitable analytical methods. This situation hinders us from employing the defect engineering approach to the soft materials. Our combination approach

based on low-dose SNBED, molecular modeling, and PiFM represents a powerful tool for revealing the structural details of soft matter defects at molecular and near-atomic resolutions. Such an approach is readily and widely applicable to various semi- and polycrystalline soft materials. A better understanding of defect structure will lead to fully exploiting the potential of soft materials, including biological and biobased materials.

EXPERIMENTAL METHODS

Detailed experimental methods are provided in the supporting information file.

ASSOCIATED CONTENT

Supporting Information. Detailed experimental methods and supplementary figures (PDF format).

AUTHOR INFORMATION

The authors declare no competing financial interests.

ACKNOWLEDGMENT

The authors acknowledge Agence Nationale de la Recherche (ANR grant number: ANR-21-CE29-0016-1) and Glyco@Alps (ANR-15-IDEX-02) for the financial support and the NanoBio-ICMG platform (FR 2607) for granting access to the electron microscopy facility. The work has benefited from characterization equipment of the Grenoble INP-CMTC platform supported by the Centre of Excellence of Multifunctional Architectured Materials 'CEMAM' n°ANR-10-LABX-44-01 funded by the Investments for the Future program.

REFERENCES

(1) J. Moon, R.; Martini, A.; Nairn, J.; Simonsen, J.; Youngblood, J. Cellulose Nanomaterials Review: Structure, Properties and Nanocomposites. *Chem. Soc. Rev.* **2011**, *40* (7), 3941–3994.

(2) Elazzouzi-Hafraoui, S.; Nishiyama, Y.; Putaux, J.-L.; Heux, L.; Dubreuil, F.; Rochas, C. The Shape and Size Distribution of Crystalline Nanoparticles Prepared by Acid Hydrolysis of Native Cellulose. *Biomacromolecules* **2008**, *9* (1), 57–65.

(3) Sacui, I. A.; Nieuwendaal, R. C.; Burnett, D. J.; Stranick, S. J.; Jorfi, M.; Weder, C.; Foster, E. J.; Olsson, R. T.; Gilman, J. W. Comparison of the Properties of Cellulose Nanocrystals and Cellulose Nanofibrils Isolated from Bacteria, Tunicate, and Wood Processed Using Acid, Enzymatic, Mechanical, and Oxidative Methods. *ACS Appl. Mater. Interfaces* **2014**, *6* (9), 6127–6138.

(4) Vasconcelos, N. F.; Feitosa, J. P. A.; da Gama, F. M. P.; Morais, J. P. S.; Andrade, F. K.; de Souza Filho, M. de S. M.; Rosa, M. de F. Bacterial Cellulose Nanocrystals Produced under Different Hydrolysis Conditions: Properties and Morphological Features. *Carbohydr. Polym.* **2017**, *155*, 425–431.

(5) Hanley, S. J.; Revol, J. F.; Godbout, L.; Gray, D. G. Atomic Force Microscopy and Transmission Electron Microscopy of Cellulose from Micrasterias Denticulata; Evidence for a Chiral Helical Microfibril Twist. *Cellulose* **1997**, *4* (3), 209–220.

(6) Frey-Wyssling, A.; Mühlethaler, K.; Muggli, R. Elementarfibrillen als Grundbausteine der nativen Cellulose. *Holz Als Roh- Werkst.* **1966**, *24* (10), 443–444.

(7) St. John Manley, R. Molecular Morphology of Cellulose. *J. Polym. Sci. Part -2 Polym. Phys.* **1971**, *9* (6), 1025–1059.

(8) Ogawa, Y. Electron Microdiffraction Reveals the Nanoscale Twist Geometry of Cellulose Nanocrystals. *Nanoscale* **2019**, *11* (45), 21767–21774.

(9) Ogawa, Y. Release of Internal Molecular Torque Results in Twists of Glaucocystis Cellulose Nanofibers. *Carbohydr. Polym.* **2021**, *251*, 117102.

(10) Usov, I.; Nyström, G.; Adamcik, J.; Handschin, S.; Schütz, C.; Fall, A.; Bergström, L.; Mezzenga, R. Understanding Nanocellulose Chirality and Structure–Properties Relationship at the Single Fibril Level. *Nat. Commun.* **2015**, *6* (1), 7564.

(11) Willhammar, T.; Daicho, K.; Johnstone, D. N.; Kobayashi, K.; Liu, Y.; Midgley, P. A.; Bergström, L.; Saito, T. Local Crystallinity in Twisted Cellulose Nanofibers. *ACS Nano* **2021**, *15* (2), 2730–2737.

(12) Dadashian, F.; Yaghoobi, Z.; Wilding, M. A. Internal Damage of Crimped Lyocell Fiber. *Text. Res. J.* **2007**, *77* (7), 457–461.

(13) Andersen, C. B.; Yagi, H.; Manno, M.; Martorana, V.; Ban, T.; Christiansen, G.; Otzen, D. E.; Goto, Y.; Rischel, C. Branching in Amyloid Fibril Growth. *Biophys. J.* **2009**, *96* (4), 1529–1536.

(14) Suenaga, K.; Wakabayashi, H.; Koshino, M.; Sato, Y.; Urita, K.; Iijima, S. Imaging Active Topological Defects in Carbon Nanotubes. *Nat. Nanotechnol.* **2007**, *2* (6), 358–360.

(15) Arcari, M.; Zuccarella, E.; Axelrod, R.; Adamcik, J.; Sánchez-Ferrer, A.; Mezzenga, R.; Nyström, G. Nanostructural Properties and Twist Periodicity of Cellulose Nanofibrils with Variable Charge Density. *Biomacromolecules* **2019**, *20* (3), 1288–1296.

(16) Nyström, G.; Arcari, M.; Adamcik, J.; Usov, I.; Mezzenga, R. Nanocellulose Fragmentation Mechanisms and Inversion of Chirality from the Single Particle to the Cholesteric Phase. *ACS Nano* **2018**, *12* (6), 5141–5148.

(17) Saito, T.; Kuramae, R.; Wohlert, J.; Berglund, L. A.; Isogai, A. An Ultrastrong Nanofibrillar Biomaterial: The Strength of Single Cellulose Nanofibrils Revealed via Sonication-Induced Fragmentation. *Biomacromolecules* **2013**, *14* (1), 248–253.

(18) Smith, K. B.; Tisserant, J.-N.; Assenza, S.; Arcari, M.; Nyström, G.; Mezzenga, R. Confinement-Induced Ordering and Self-Folding of Cellulose Nanofibrils. *Adv. Sci.* **2019**, *6* (4), 1801540.

(19) Manley, R. S.-J. Kinking in Cellulose Microfibrils. *Text Res J* **1974**, *44* (8), 637–638.

(20) Chanzy, H.; Henrissat, B. Undirectional Degradation of Valonia Cellulose Microcrystals Subjected to Cellulase Action. *FEBS Lett.* **1985**, *184* (2), 285–288.

(21) Ciesielski, P. N.; Wagner, R.; Bharadwaj, V. S.; Killgore, J.; Mittal, A.; Beckham, G. T.; Decker, S. R.; Himmel, M. E.; Crowley, M. F. Nanomechanics of Cellulose Deformation Reveal Molecular Defects That Facilitate Natural Deconstruction. *Proc. Natl. Acad. Sci.* **2019**, *116* (20), 9825–9830.

(22) Zhou, Y.; Ono, Y.; Takeuchi, M.; Isogai, A. Changes to the Contour Length, Molecular Chain Length, and Solid-State Structures of Nanocellulose Resulting from Sonication in Water. *Biomacromolecules* **2020**, *21* (6), 2346–2355.

(23) Chen, P.; Ogawa, Y.; Nishiyama, Y.; Ismail, A. E.; Mazeau, K. Linear, Non-Linear and Plastic Bending Deformation of Cellulose Nanocrystals. *Phys. Chem. Chem. Phys.* **2016**, *18* (29), 19880–19887.

(24) Schwarzer, R. A.; Sukkau, J. Automated Crystal Orientation Mapping (ACOM) with a Computer-Controlled TEM by Interpreting Transmission Kikuchi Patterns. *Mater. Sci. Forum* **1998**, *273–275*, 215–222.

(25) Rauch, E. F.; Véron, M. Automated Crystal Orientation and Phase Mapping in TEM. *Mater. Charact.* **2014**, *98*, 1–9.

(26) Ophus, C. Four-Dimensional Scanning Transmission Electron Microscopy (4D-STEM): From Scanning Nanodiffraction to Ptychography and Beyond. *Microsc. Microanal.* **2019**, *25* (3), 563–582.

(27) Bustillo, K. C.; Zeltmann, S. E.; Chen, M.; Donohue, J.; Ciston, J.; Ophus, C.; Minor, A. M. 4D-STEM of Beam-Sensitive Materials. *Acc. Chem. Res.* **2021**, *54* (11), 2543–2551.

(28) Gallagher-Jones, M.; Ophus, C.; Bustillo, K. C.; Boyer, D. R.; Panova, O.; Glynn, C.; Zee, C.-T.; Ciston, J.; Mancia, K. C.; Minor, A. M.; Rodriguez, J. A. Nanoscale Mosaicity Revealed in Peptide Microcrystals by Scanning Electron Nanodiffraction. *Commun. Biol.* **2019**, *2* (1), 26.

(29) Panova, O.; Chen, X. C.; Bustillo, K. C.; Ophus, C.; Bhatt, M. P.; Balsara, N.; Minor, A. M. Orientation Mapping of Semicrystalline Polymers Using Scanning Electron Nanobeam Diffraction. *Micron* **2016**, *88*, 30–36.

(30) Nishiyama, Y.; Langan, P.; Chanzy, H. Crystal Structure and Hydrogen-Bonding System in Cellulose Iβ from Synchrotron X-Ray and Neutron Fiber Diffraction. *J. Am. Chem. Soc.* **2002**, *124* (31), 9074–9082.

(31) Helbert, W.; Nishiyama, Y.; Okano, T.; Sugiyama, J. Molecular Imaging of Halocynthia Papillosa Cellulose. *J. Struct. Biol.* **1998**, *124* (1), 42–50.

(32) Briois, B.; Saito, T.; Pétrier, C.; Putaux, J.-L.; Nishiyama, Y.; Heux, L.; Molina-Boisseau, S. Iα → Iβ Transition of Cellulose under Ultrasonic Radiation. *Cellulose* **2013**, *20* (2), 597–603.

(33) Wu, X.; Zhou, R.; Yang, J.; Zeng, X. C. Density-Functional Theory Studies of Step-Kinked Carbon Nanotubes. *J. Phys. Chem. C* **2011**, *115* (10), 4235–4239.

(34) Chanzy, H. Irradiation de La Cellulose de Valonia Au Microscope à 1 MV. *BIST Commis. Energ. At.* **1975**, 55–57.

(35) Hou, Y.; He, Z.; Zhu, Y.; Wu, H. Intrinsic Kink Deformation in Nanocellulose. *Carbohydr. Polym.* **2021**, *273*, 118578.

(36) Frka-Petesic, B.; Sugiyama, J.; Kimura, S.; Chanzy, H.; Maret, G. Negative Diamagnetic Anisotropy and Birefringence of Cellulose Nanocrystals. *Macromolecules* **2015**, *48* (24), 8844–8857.

(37) Chen, P.; Ogawa, Y.; Nishiyama, Y.; Ismail, A. E.; Mazeau, K. Iα to Iβ Mechano-Conversion and Amorphization in Native Cellulose Simulated by Crystal Bending. *Cellulose* **2018**, *25* (8), 4345–4355.

(38) Nowak, D.; Morrison, W.; Wickramasinghe, H. K.; Jahng, J.; Potma, E.; Wan, L.; Ruiz, R.; Albrecht, T. R.; Schmidt, K.; Frommer, J.; Sanders, D. P.; Park, S. Nanoscale Chemical Imaging by Photoinduced Force Microscopy. *Sci. Adv.* **2016**, *2* (3), e1501571.

(39) Marchessault, R. H.; Morehead, F. F.; Koch, M. J. Some Hydrodynamic Properties of Neutral Suspensions of Cellulose Crystallites as Related to Size and Shape. *J. Colloid Sci.* **1961**, *16* (4), 327–344.

(40) Kotov, N.; Larsson, P. A.; Jain, K.; Abitbol, T.; Cernescu, A.; Wågberg, L.; Johnson, C. M. Elucidating the Fine-Scale Structural Morphology of Nanocellulose by Nano Infrared Spectroscopy. *Carbohydr. Polym.* **2023**, *302*, 120320.

(41) Hess, K. M.; Killgore, J. P.; Mittal, A.; Srubar, W. V. Viscoelastic-Mapping of Cellulose Nanofibrils Using Low-Total-Force Contact Resonance Force Microscopy (LTF-CRFM). *Cellulose* **2022**, *29* (10), 5493–5509.

(42) Jarvis, M. C. Interconversion of the Iα and Iβ Crystalline Forms of Cellulose by Bending. *Carbohydr. Res.* **2000**, *325* (2), 150–154.

(43) Horii, F.; Hirai, A.; Yamamoto, H. Microstructural Analysis of Microfibrils of Bacterial Cellulose. *Macromol. Symp.* **1997**, *120* (1), 197–205.